# Supporting information

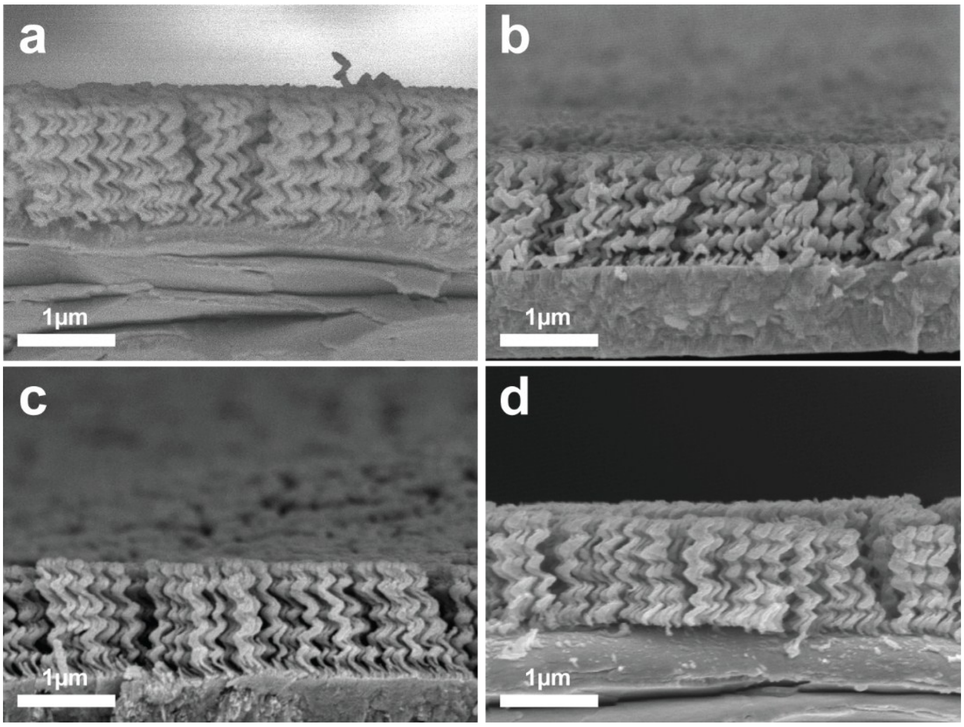

**Fig. S1**. SEM images of the samples before and after the annealing process. (a) As-deposited $WO_3$, (b) Air-$WO_3$, (c) Ar-$WO_3$ and (d) $H_2$-$WO_3$.

## X-ray diffraction (XRD) and Raman spectroscopy

The growth of $WS_2$ from $WO_3$ NHs by the sulfurization was confirmed by X-ray diffraction (XRD) and Raman spectroscopy. As shown in Fig. S2a, the characteristic XRD peaks of $WS_2$ (JCPDS #08-0237) appear near 14 ° after the sulfurization together with the peaks from $WO_3$ (JCPDS #43-1035) and W foil. Raman spectroscopy was also performed to identify the characteristics of the $WS_2$ grown on three samples as shown in Fig. S2b. All the samples show characteristic Raman scattering peaks of $WS_2$ $A_{1g}$ at 420 $cm^{-1}$ representing the out-of-plane W-S phonon mode and $E^1_{2g}$ at 354 $cm^{-1}$ for the in-plane W-S phonon mode,[1] confirming the formation of $WS_2$ by the sulfurization.

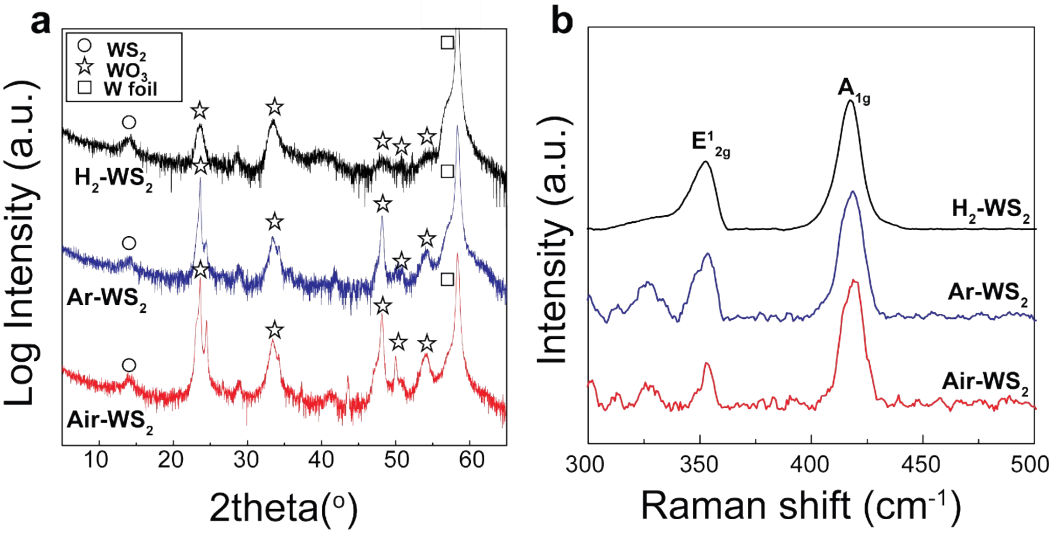

**Fig. S2**. Material characterization of fabricated $WS_2/WO_3$ samples. (a) XRD patterns and (b) Raman spectra of each sample (Air, Ar and $H_2$-$WS_2$)

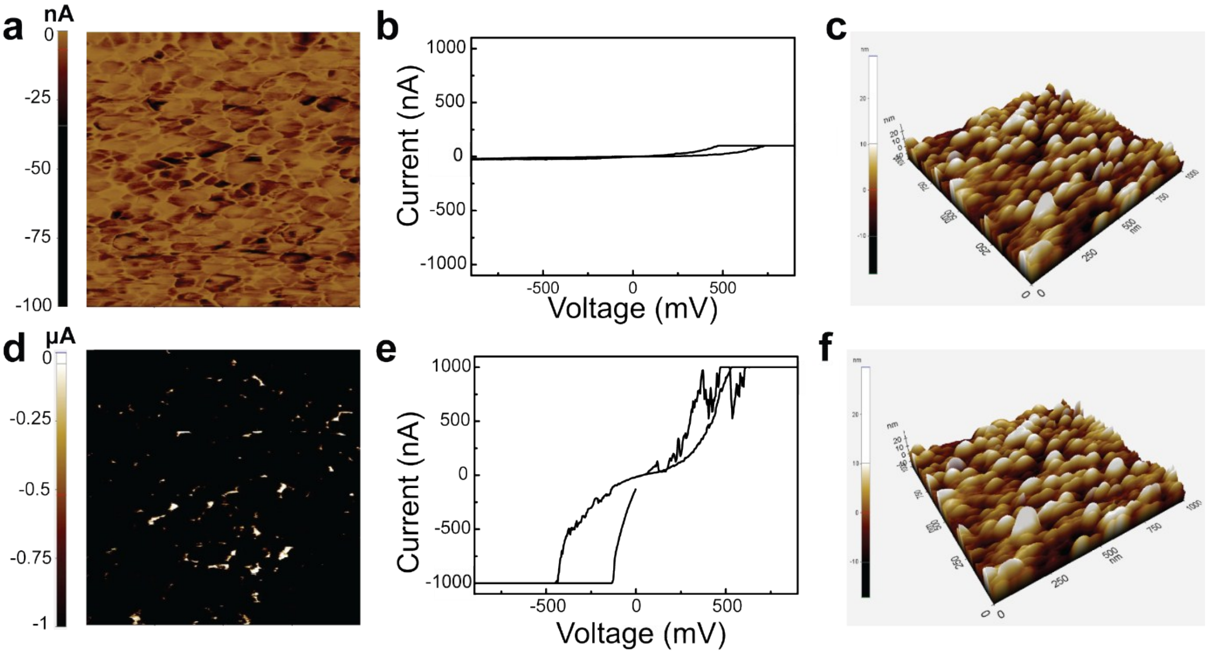

**Fig. S3.** Conductive atomic force microscopy (CAFM) results of (a) – (c) Air-$WO_3$ and (d) – (f) $H_2$-$WO_3$. (a) and (d) show the conductivity mapping. (b) and (e) show the I-V curve. (c) and (f) show the surface morphology of the samples. The $H_2$-$WO_3$ shows much higher conductivity compared with the Air-$WO_3$.

## DFT calculation

First-principles density functional theory (DFT) calculations were performed to understand how the annealing in $H_2$ atmosphere change the growth behavior of $WS_2$ on $WO_3$ surface during the sulfurization. Based on the DFT calculations, the (100) plane with $(\sqrt{2}\times\sqrt{2})R45^\circ$ surface reconstruction is identified as the most energetically favorable surface termination of the $WO_3$ slab as shown in Fig. 3a.[2,3] The surface structure is constructed by $2\sqrt{2}\times2\sqrt{2}$ supercell with 8 atoms so that 4 W ions and 4 O ions are placed on the surface. Since strong adsorption of disulfur ($S_2$) molecule can expedite the sulfurization of the $WO_3$ surface, the binding energy of $S_2$ molecule on the $WO_3$ surface was investigated. Since the surface oxygen ions can be reduced by hydrogen annealing, we additionally created reduced surface to reflect the oxygen deficient condition in which the half of the oxygen ions are removed from the surface. Fig. 3a and b show the schematic views of normal and reduced structure of $WO_3$ surface. Our DFT calculations predict that the binding of $S_2$ molecule is significantly enhanced on the reduced surface; the binding energy is increased from 0.505 eV (normal) to 1.066 eV (reduced) as shown in the Fig. 1e and 1f. The charge density distribution of $S_2$ molecule on two different surfaces was further investigated in order to understand the physical origin of the enhanced binding of $S_2$ on the reduced surface. As can be seen from Fig. 3e, $S_2$ molecule is weakly adsorbed on $WO_3$ surface because of steric hindrance of dense dangling oxygen. On the other hand, $S_2$ molecule binds strongly with two W ions and form a bridge shape configuration on the reduced surface, as shown in Fig. 3f. As a result, $S_2$ molecule binds more strongly with reduced $WO_3$ surface. The enhanced binding of $S_2$ molecule on the reduced surface is reasonable since electronegative $S_2$ molecule should prefer the reduced surface. Note that this growth mechanism can be applied to other experimental studies such as space-confined growth of $MoS_2$[4] or hierarchically nanostructured $MoS_2$[5]. Based on the DFT calculation, the oxygen deficiency induced by the annealing in $H_2$ atmosphere can facilitate the nucleation, and accelerate the growth of $WS_2$ and thus sporadic and thick $WS_2$ layer is observed for the $H_2$-$WS_2$ sample, causing the formation of a rich edge-exposed $WS_2$.

**Table S1.** Calculated energies for each system with the $S_2$ adsorption

| System | Surface reaction | Energy (eV) | Adsorption (eV) | Note |
|---|---|---|---|---|
| **$S_2$** |  | -7.100 |  | Spin-polarization |
| **Normal** |  | -613.894 |  |  |
| **$S_2$-$W_N$** | $S_2$ + Normal → $S_2$-$W_N$ | -621.500 | -0.505 | Steric hindrance |
| **Reduced** |  | -600.547 |  |  |
| **$S_2$-$W_R$** | $S_2$ + Reduced → $S_2$-$W_R$ | -608.712 | -1.065 | Bridge binding |
| **$S_2$-$W_R^*$** | $S_2$ + Reduced → $S_2$-$W_R^*$ | -608.713 | -1.066 | Bridge binding |

$S_2$ is a disulfide system which magnetization is $2\mu_B$, Normal and Reduced are symmetric slab models of normal and reduced surface state, and the energy is half value of full system. $S_2$-$W_N$ is adsorption system from normal surface state. $S_2$-$W_R$ and $S_2$-$W_R^*$ are adsorption systems from reduced surface state with 'same' and 'different' adsorption site of $S_2$-$W_N$.

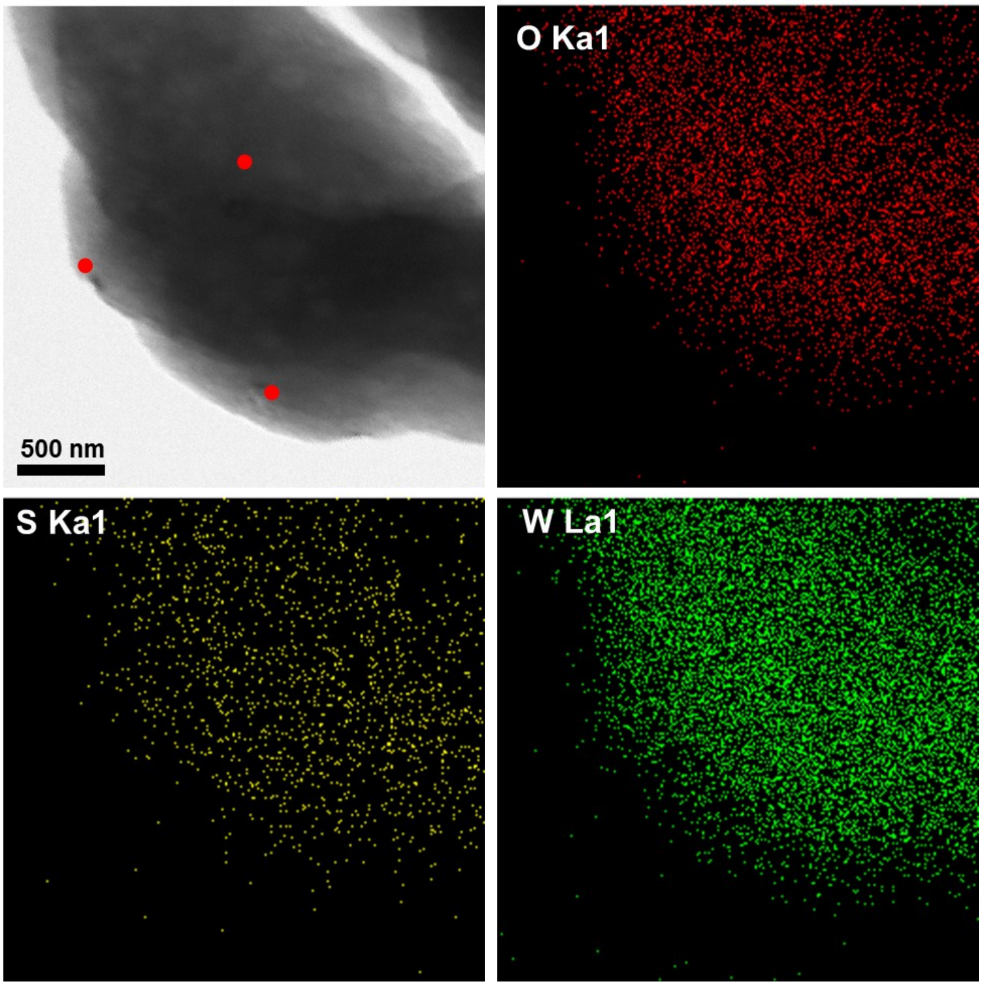

**Fig. S4.** TEM images and elemental mapping of O, S and W collected by EDS analysis from Air-$WS_2$ sample. Average atomic percent collected from three red dots in TEM images is summarized in Table S2.

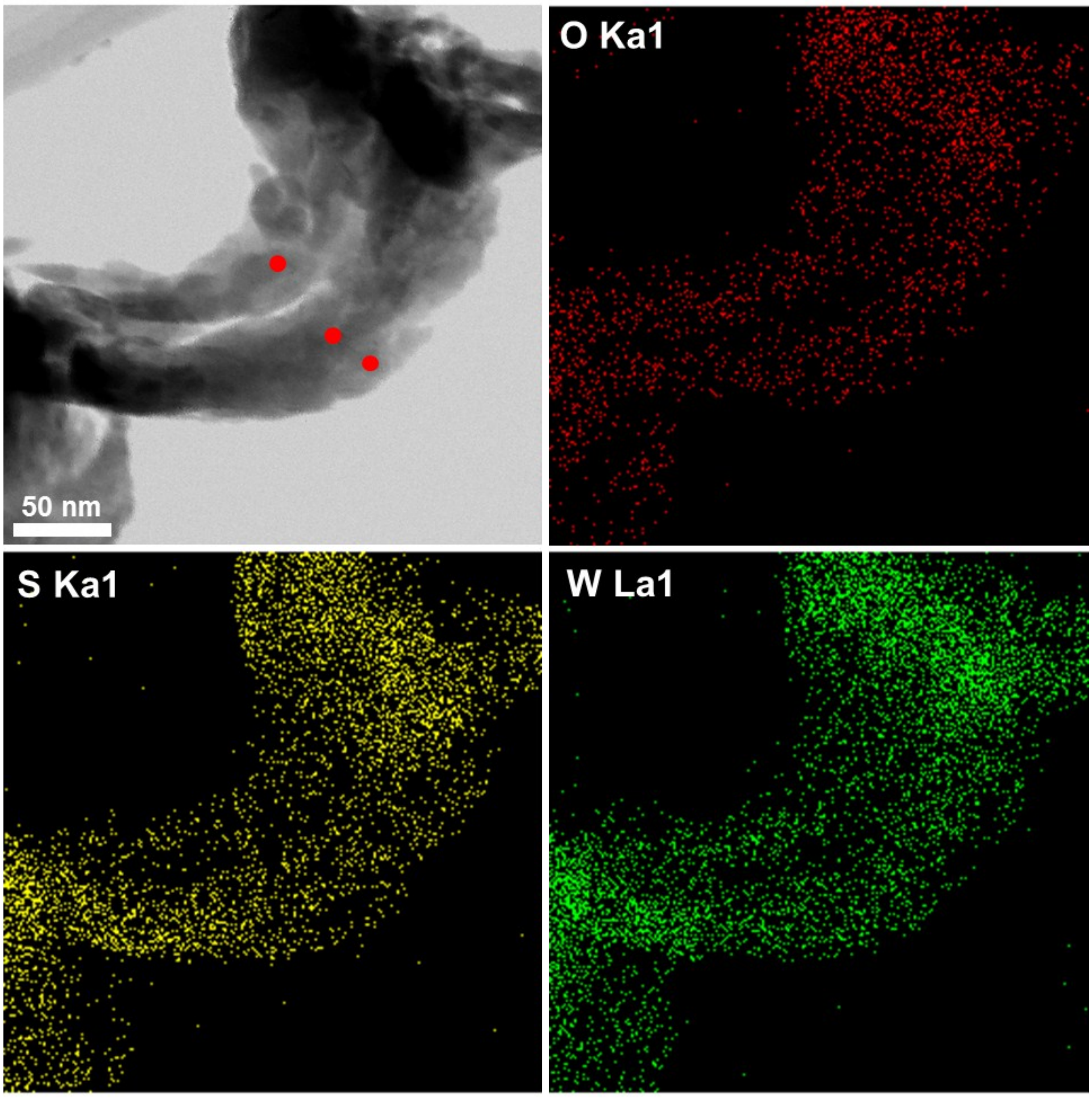

**Fig. S5.** TEM images and elemental mapping of O, S and W collected by EDS analysis from $H_2$-$WS_2$ sample. Average atomic percent collected from three red dots in TEM images is summarized in Table S2.

**Table S2**. Average atomic percent of O, S and W collected from Air-$WS_2$ and $H_2$-$WS_2$. Three red dots in each TEM images show the spot where the spectrum was collected

| **Elements** | **Air-$WS_2$ (Average atomic %)** | **$H_2$-$WS_2$ (Average atomic %)** |
|---|---|---|
| O K | 50.53 | 32.36 |
| S K | 2.48 | 28.33 |
| W L | 46.98 | 39.31 |

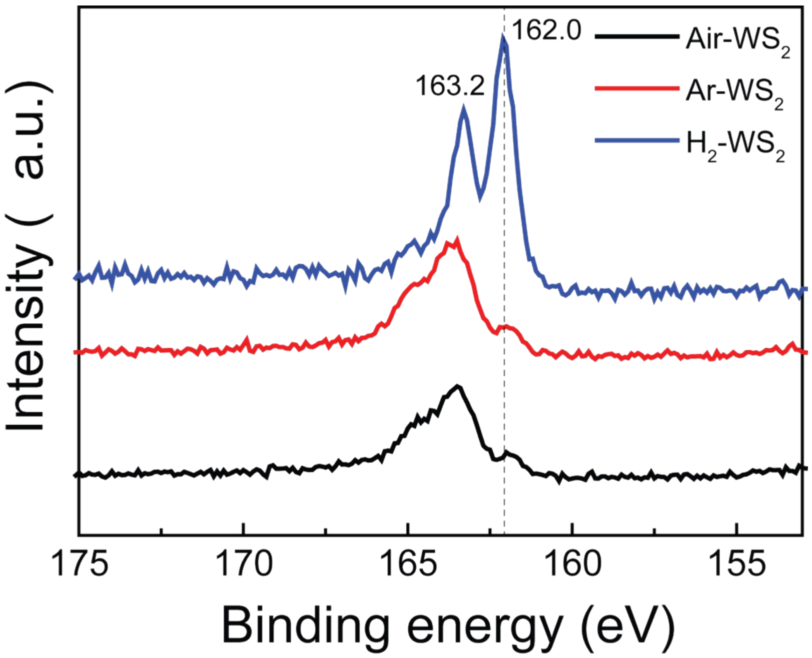

**Fig. S6.** S2p XPS spectra from the samples of Air-$WS_2$, Ar-$WS_2$ and $H_2$-$WS_2$.

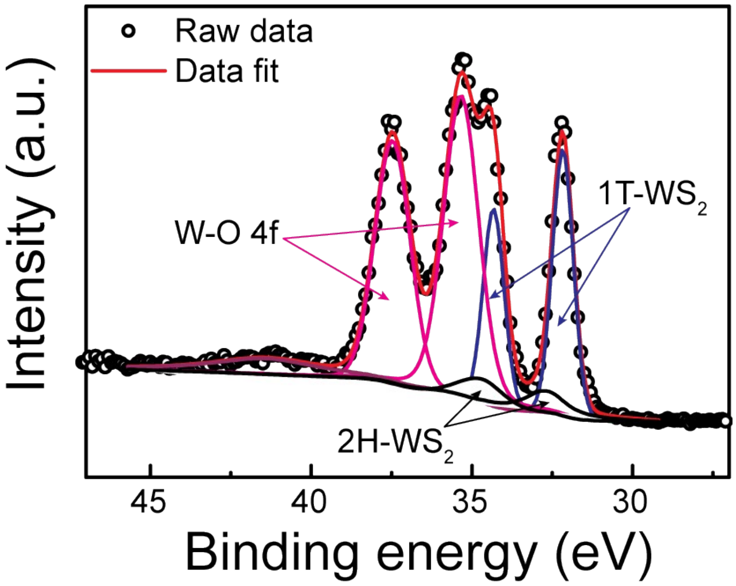

**Fig. S7.** W4f XPS spectra of the $H_2$-$WS_2$ sample deconvoluted into 1T and 2H phase $WS_2$.

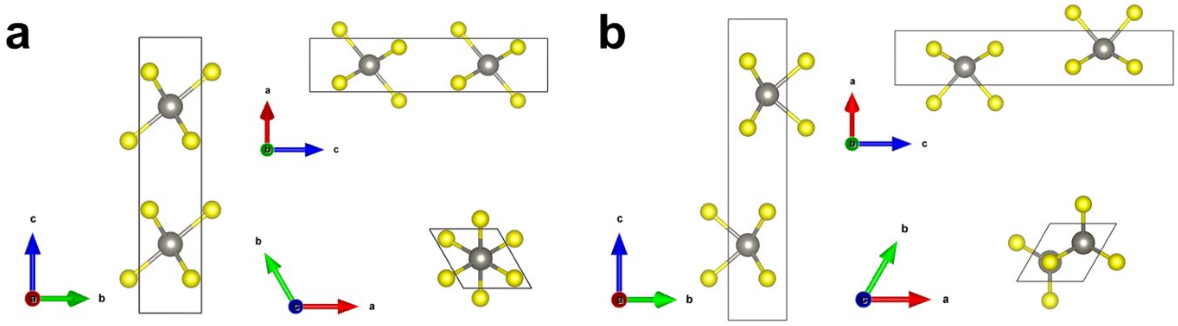

**Fig. S8.** Atomic unit cell structure model used for HREM simulation. (a) 1T phase WS$_2$ and (b) 2H phase WS$_2$ with various perspective view.[6–8]

## Crystallographic information file (CIF) of the 1T-WS$_2$.[6,7]

Generated by ‘Crystal Maker’

Unit cell_a = 3.21 Å

Unit cell_b = 3.21 Å

Unit cell_c = 6.18 Å

Unit cell_α = 90°

Unit cell_β = 90°

Unit cell_γ = 120°

Space group = P -3 m 1

**Atomic position (x, y, z)**

| | | | |
|---|---|---|---|
| S1 | 0.833300 | 0.166700 | 0.875000 |
| S1 | 0.166700 | 0.833300 | 0.125000 |
| S1 | 0.166700 | 0.833300 | 0.625000 |
| S1 | 0.833300 | 0.166700 | 0.375000 |
| W1 | 0.500000 | 0.500000 | 0.750000 |
| W1 | 0.500000 | 0.500000 | 0.250000 |

### CIF file of the 2H-$WS_2$.[6,8]

We use the Material Project database for CIF of 2H phase $WS_2$ (mp-224)

**https://materialsproject.org/**

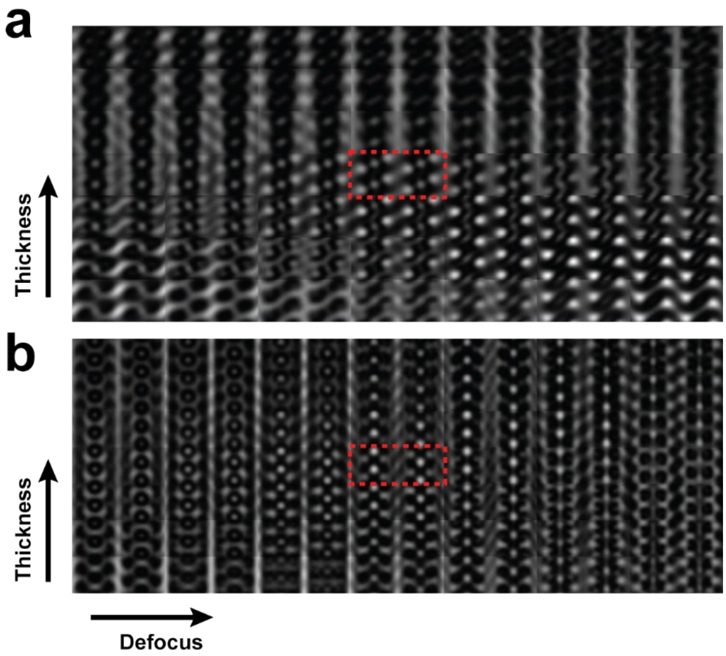

**Fig. S9.** HREM simulation mapping results for (a) 1T phase and (b) 2H phase $WS_2$ by changing the defocusing and thickness. *y* axis for each data means the thickness change (a) from 5.46 nm to 24.72 nm and (b) from 42.38 nm to 61.64 nm with 3.21 nm interval. *x* axis means the change in the defocusing (a) from 28.4 nm to 58.4 nm and (b) from 38.4 nm to 68.4 nm with 5 nm interval. Red dotted square denotes the simulation data that coincide with experimental data. Scherzer defocus is 43.4 nm.

## Strain caused by 3D scaffold $WO_3$

For investigating the effect of curved 3D $WO_3$ scaffold, $WO_3$ film structure with 1 μm thickness was fabricated followed by $H_2$ annealing and sulfurization using the same fabrication condition of $H_2$-$WS_2$, denoted as $H_2$-$WS_2$ (TF) (Fig. S10a and S10b). As implied in the XRD data (Fig. S10c), $WS_2/WO_3$ was successfully fabricated. The W4f binding energies of $WS_2$ in each sample ($H_2$-$WS_2$ and $H_2$-$WS_2$ (TF)) were compared in the XPS data (Fig. S10d). As shown in the XPS data, $WS_2$ in the NH system shows lower binding energy compared to $WS_2$ in the film system, which implies that the curvature-induced strain from curved 3D NH affects to the bonding state of $WS_2$.

Furthermore, difference in the thermal expansion coefficient (TEC) between $WO_3$ and $WS_2$ induces the thermal strain on the $WS_2$ during the cooling after the CVD growth. It was previously studied that the TEC difference between substrate and TMDCs causes the strain and even induce the phase transition during the CVD process.[9–11] According to the previous reports, TEC difference of $WS_2$ ($6.5 \cdot 10^{-6}$ $K^{-1}$) and $WO_3$ ($11 \sim 13 \cdot 10^{-6}$ $K^{-1}$) is enough to activate the phase transition.[11,12] The result of XPS and HRTEM data, which is well-known method to identify the two polymorphs (2H and 1T) of TMDCs, shows the characteristics of 1T phase $WS_2$ by exhibiting binding energies at 32.2 and 34.3 eV.

**Table S3.** Lattice parameters of $WS_2$[7,8,13] and $WO_3$ (JCPDS #43-1035).

| | $WO_3$ | 2H phase $WS_2$ | 1T phase $WS_2$ |
|---|---|---|---|
| a (Å) | 7.309 | 3.18 | 3.21 |
| b (Å) | 7.522 | 3.18 | 3.21 |
| c (Å) | 7.678 | 12.27 | 6.18 |
| α (°) | 88.81 | 90 | 90 |
| β (°) | 90.92 | 90 | 90 |
| γ (°) | 90.93 | 120 | 120 |

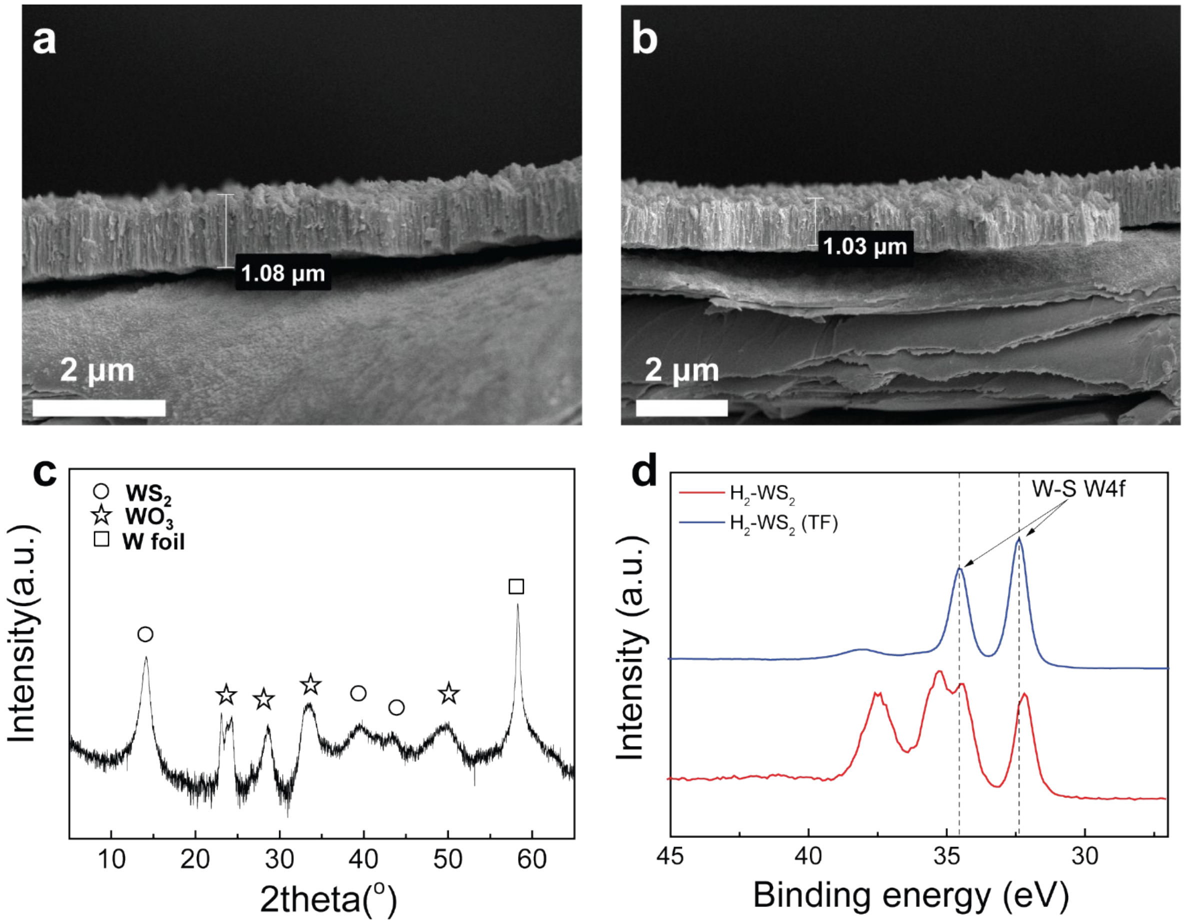

**Fig. S10.** (a), (b) SEM images of 1µm thick sulfurized thin film $WS_2/WO_3$ ($H_2$-$WS_2$ (TF)) on W foil. (c) XRD patterns of $H_2$-$WS_2$ (TF) and (d) normalized XPS spectra of W4f comparing $H_2$-$WS_2$ NH and $H_2$-$WS_2$ thin film system. The binding energy of NH is lower than the thin film.

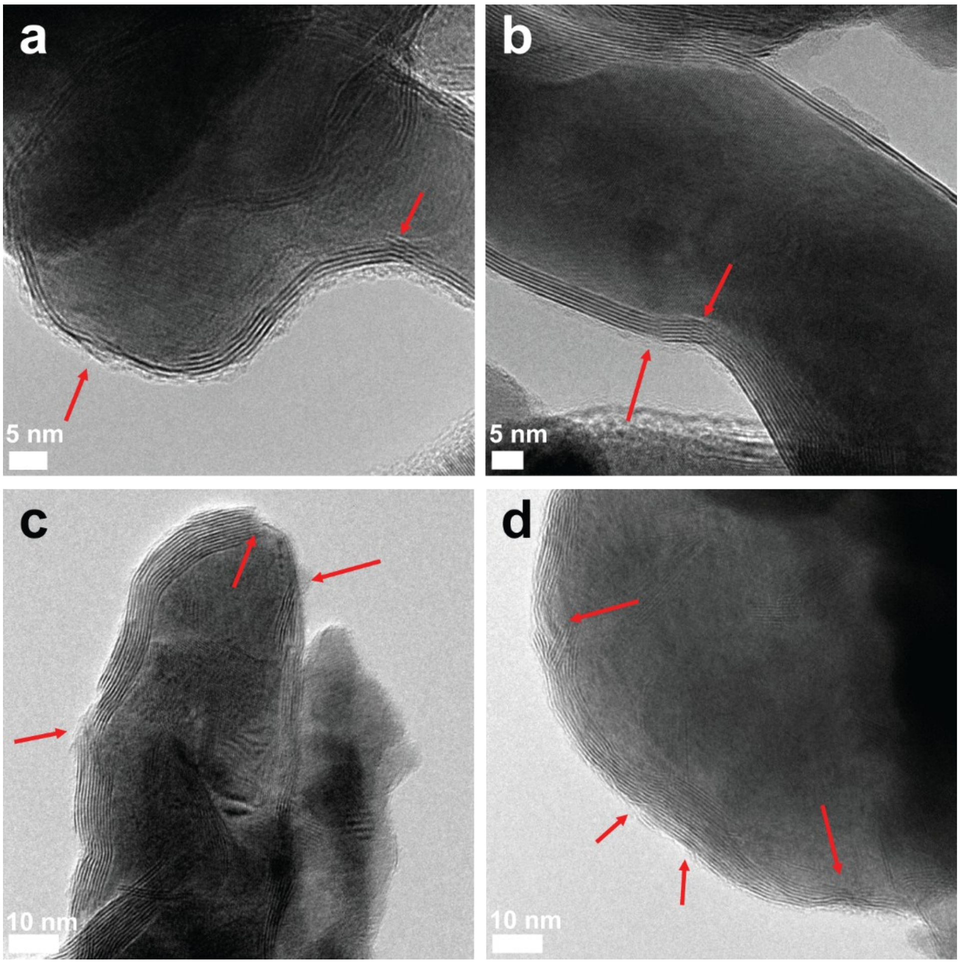

**Fig. S11.** The TEM images of (a), (b) Air-$WS_2$ and (c), (d) $H_2$-$WS_2$. Red arrows show the exposed edge by the distorted and defective site of TMDC manifested at the curved surface

## Faradaic efficiency and XPS analysis after the stability test

Additional XPS analysis was carried out for the $H_2$-$WS_2$ sample after the stability test. As shown in Fig. S12, W4f and S2p peak intensity from $WS_2$ is reduced compared to those from the pristine $H_2$-$WS_2$ sample. On the other hand, a new peak, indexed as S2p from $(SO_4)^{2-}$ bonding[14], appeared after the stability test, which is attributed to the formation of electrochemical reaction product between the electrode and the electrolyte. It is believed that the surface of the sample is partially oxidized[15] and/or covered by the reaction product after taking it out from the electrolyte after the stability test, resulting in reduced peak intensity from $WS_2$. Note that XPS is a surface sensitive characterization tool due to very low photoelectron escape depth. Nevertheless, HER activity is maintained after the stability test. In addition, faradaic efficiency (FE) for hydrogen from the HER was analyzed with the $H_2$-$WS_2$ sample after the stability test, showing the 96% of FE at −0.168 $V_{RHE}$. (Details of experiment for FE are explained in Fig. S14)"

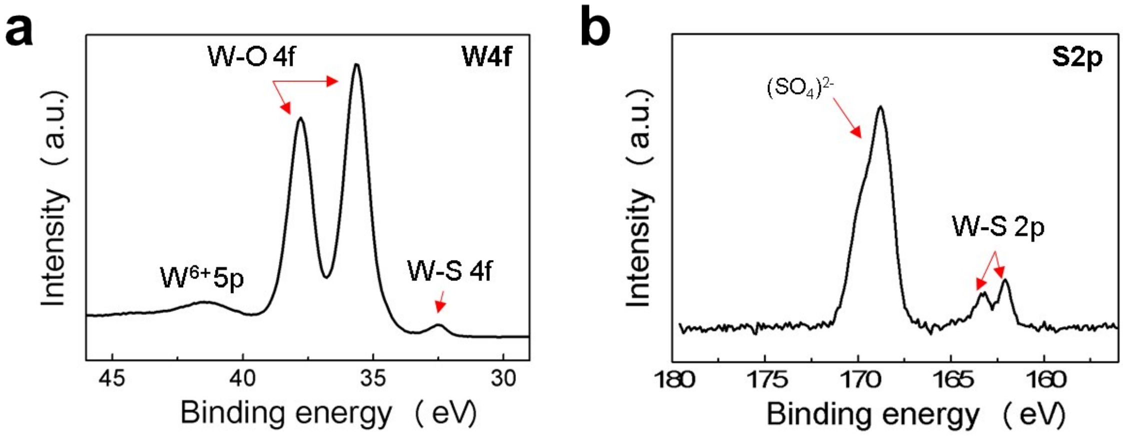

**Fig. S12**. XPS spectra of the sample after stability test. (a) W4f spectra and (b) S2p spectra

## Tafel slope

We have tried to obtain the Tafel slopes from the polarization curves of the three electrodes shown in Fig. S13. However, a significant additional reduction current before the onset potential was observed as shown in Fig. S13b, which makes it difficult to evaluate the Tafel slopes as well as onset potentials accurately. As shown in Fig. S13c, the Tafel slopes obtained from the polarization curves are abnormally high compared to previously reported values due to such additional reduction currents that can be associated with electrochromic reaction of $WO_3$ to form $H_xWO_3$ near − 0.1 V (vs. RHE) which overlaps with the onset potential region of our samples (− 0.15 ~ − 0.05 V vs. RHE).[16]

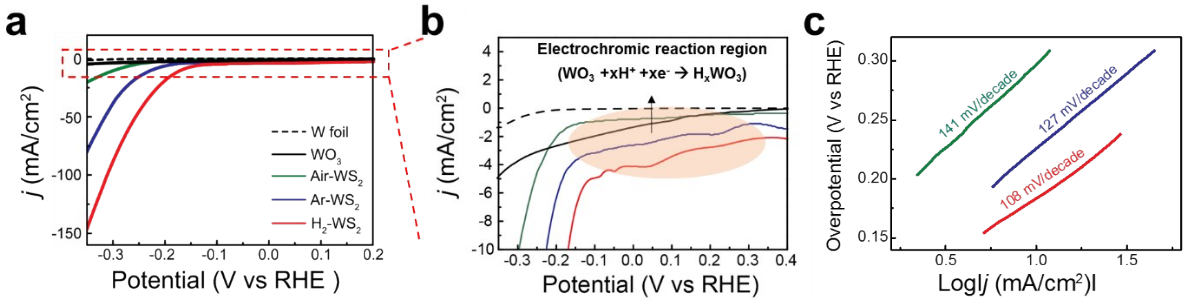

**Fig. S13.** (a) Polarization curves for HER and (b) magnified image adjacent to the onset potential of (a). (c) Tafel plots and slopes of the fabricated samples corresponding to the polarization curves.

### Faradaic efficiency (FE) of HER

To evaluate the electrochemical catalytic ability to catalyze HER and exclude the effect of electrochromic reaction, the faradaic efficiency (FE) of HER was calculated. The electrochemical test was carried out in the H-type electrochemical cell and the produced hydrogen was analyzed with gas chromatography (GC, Agilent 7890B). The system consists of the H-type cell filled with the electrolyte, working electrode, counter electrode and reference electrode. The Ar is supplied to the cell as a carrier gas and carries the produced hydrogen to the GC.

The chronoamperometric measurements was carried out adjacent to the onset potential. After 20 min of the reaction, the concentration of produced hydrogen is analyzed with the GC. From the results, the FE was calculated using Equation (1). In equation (1), $\alpha$ represents the number of electrons transferred to produce $H_2$ ($\alpha = 2$ in HER), $n$ is the number of mole of produced $H_2$, $F$ is Faraday's constant (96485 C/mol) and $Q$ represents the total charge passed.[17,18]

$$\text{Faradaic efficiency} = \frac{\alpha\, n\, F}{Q} = \frac{\text{Gas flow through cell} \times \text{Concentration of Product}}{\dfrac{\text{Current at sampling time}}{\alpha F}} \times 100 \qquad (1)$$

As shown in Fig. S14, the FE at − 0.168 $V_{RHE}$ is nearly 90%, which implies that a small part of total current originates from the electrochromic reaction of $WO_3$. At − 0.2 $V_{RHE}$, however, the FE of hydrogen is 96.4% indicating a negligible electrochromic reaction. As a result, it can be inferred that the electrochemical current in Fig. 5a originates from the $H_2$ production.

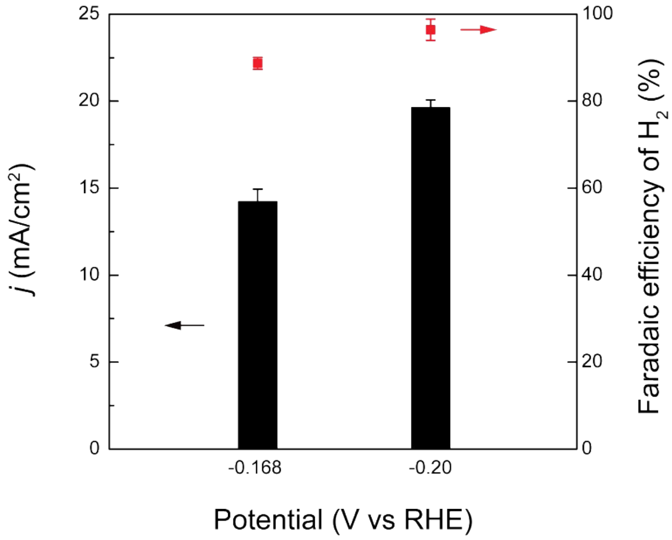

**Fig. S14.** Current density and faradaic efficiency obtained after 20 min of chronoamperometric measurements.

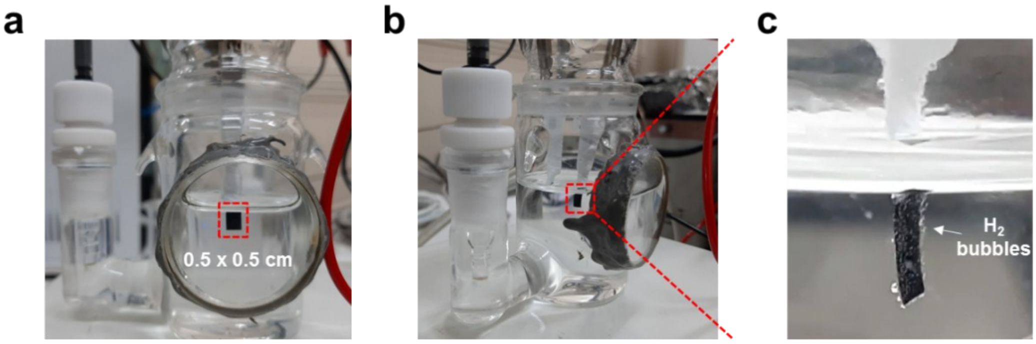

**Fig. S15.** Pictures of the electrochemical cell system with (a) front and (b) side view. (c) Picture of evolved hydrogen bubbles at the surface of working electrode (−0.3 $V_{RHE}$).

**Table S4** Comparison of electrochemical performance for different samples

| **Samples** | **Onset potential [mV]** | **Tafel slope [mV/dec]** | **Overpotential (mV) at 10 mA/cm$^2$** | **$R_{CT}$ [Ω]** | **Ref** |
|---|---|---|---|---|---|
| Vertically aligned $WS_2$ | − 0.03 | 61 | − 0.136 | N/A | 19) |
| Vertically oriented $WS_2$ | N/A | 105 | N/A | N/A | 20) |
| Exfoliated $WS_2$ | ~ − 0.12 | ~90 | ~ − 0.4 | N/A | 21) |
| Microwave exfoliated $WS_2$ | − 0.075 | 70 | − 0.142 | 5 | 22) |
| Exfoliated $WS_2$ | − 0.03~0.06 | 60 | N/A | N/A | 23) |
| Exfoliated-$WS_2$ | N/A | 85 | ~ − 0.035 | N/A | 24) |
| BuLi exfoliated $WS_2$ | − 0.31 | ~110 | ~ − 0.7 | N/A | 25) |
| $WS_2$/P,N,O-graphene | N/A | 52.7 | − 0.125 | 6.5 | 26) |
| $WS_2$/rGO | − 0.15 ~ − 0.2 | 58 | N/A | ~200 | 27) |
| rGO/$WS_2$ | N/A | 73 | − 0.229 | 31.6 | 28) |
| $WS_{2(1-x)}P_{2x}$ nanoribbon | N/A | 71 | − 0.98 | 2.78 | 29) |
| $H_2O$ quenched $WS_2$ nanoribbon | − 0.15 | 68 | − 0.225 | 38 | 30) |
| $WS_2$ nanosheet | − 0.06 | 72 | > − 0.15 | N/A | 31) |
| $WS_2$ nanosheet/nanodot | − 0.18 | 75 | N/A | N/A | 32) |
| N-doped $WS_2$ nanosheet | − 0.86 | 82.55 | N/A | 39 | 33) |
| $WS_2$ nanoflake | − 0.1 | 48 | N/A | N/A | 34) |
| Exfoliate $WS_2$ nanodot | − 0.09 | 51 | N/A | N/A | 35) |
| $WS_{2(1-x)}Se_{2x}$ nanotube (x = 0.52) | N/A | e | N/A | 204 | 36) |
| $WS_{2(1-x)}Se_{2x}$ nanoribbon | N/A | 68 | 0.173 | 50 | 37) |
| Hierarchical $WS_2$ | 32 | 60 | 0.157 | N/A | 38) |
| Edge exposed 1T-$WS_2$ | < − 0.1 | N/A | − 0.168 | 8 | This work |

## Reference

1 Y. Yang, H. Fei, G. Ruan, Y. Li and J. M. Tour, *Adv. Funct. Mater.*, 2015, **25**, 6199–6204.

2 C. Lambert-Mauriat, V. Oison, L. Saadi and K. Aguir, *Surf. Sci.*, 2012, **606**, 40–45.

3 R. E. Tanner and E. I. Altman, *J. Vac. Sci. Technol. A*, 2001, **19**, 1502–1509.

4 X. Zheng, J. Xu, K. Yan, H. Wang, Z. Wang and S. Yang, *Chem. Mater.*, 2014, **26**, 2344–2353.

5 H. Huang, L. Chen, C. Liu, X. Liu, S. Fang, W. Liu and Y. Liu, *J. Mater. Chem. A*, 2016, **4**, 14577–14585.

6 B. Ouyang, G. Lan, Y. Guo, Z. Mi and J. Song, *Appl. Phys. Lett.*, 2015, **107**, 191903.

7 R. J. Toh, Z. Sofer, J. Luxa, D. Sedmidubský and M. Pumera, *Chem. Commun.*, 2017, **53**, 3054–3057.

8 A. Jain, S. P. Ong, G. Hautier, W. Chen, W. D. Richards, S. Dacek, S. Cholia, D. Gunter, D. Skinner, G. Ceder and K. A. Persson, *APL Mater.*, 2013, **1**, 011002..

9 Z. Liu, M. Amani, S. Najmaei, Q. Xu, X. Zou, W. Zhou, T. Yu, C. Qiu, A. G. Birdwell, F. J. Crowne, R. Vajtai, B. I. Yakobson, Z. Xia, M. Dubey, P. M. Ajayan and J. Lou, *Nat. Commun.*, 2014, **5**, 5246.

10 G. H. Ahn, M. Amani, H. Rasool, D. H. Lien, J. P. Mastandrea, J. W. Ager, M. Dubey, D. C. Chrzan, A. M. Minor and A. Javey, *Nat. Commun.*, 2017, **8**, 608.

11 Z. Wang, Y. Shen, Y. Ito, Y. Zhang, J. Du, T. Fujita, A. Hirata, Z. Tang and M. Chen,

*ACS Nano*, 2018, **12**, 1571–1579.

12 C. Rosen, E. Banks and B. Post, *Acta Crystallogr.*, 1956, **9**, 475–476.

13 R. J. Toh, Z. Sofer, J. Luxa, D. Sedmidubsky and M. Pumera, *Chem. Commun.*, 2017, **21**, 3054–3057

14 L. R. Arcot, M. Lundahl, O. J. Rojas and J. Laine, *Cellulose*, 2014, **21**, 4209–4218.

15 Z. Liu, N. Li, C. Su, H. Zhao, L. Xu, Z. Yin, J. Li and Y. Du, *Nano Energy*, 2018, **50**, 176–181.

16 S. Darmawi, S. Burkhardt, T. Leichtweiss, D. A. Weber, S. Wenzel, J. Janek, M. T. Elm and P. J. Klar, *Phys. Chem. Chem. Phys.*, 2015, **17**, 15903–15911

17 L. Zhang, Z. J. Zhao and J. Gong, *Angew. Chemie. Int. Ed.*, 2017, **56**, 11326–11353.

18 G. O. Larrazábal, A. J. Martín, S. Mitchell, R. Hauert and J. Pérez-Ramírez, *ACS Catal.*, 2016, **6**, 6265–6274.

19 Y. Yang, H. Fei, G. Ruan, Y. Li and J. M. Tour, *Adv. Funct. Mater.*, 2015, **25**, 6199–6204.

20 Y. Yan, B. Xia, N. Li, Z. Xu, A. Fisher and X. Wang, *J. Mater. Chem. A*, 2015, **3**, 131–135.

21 X. Chia, A. Ambrosi, Z. Sofer, J. Luxa and M. Pumera, *ACS Nano*, 2015, **9**, 5164–5179.

22 M. a Lukowski, A. S. Daniel, C. R. English, F. Meng, A. Forticaux, R. J. Hamers and S. Jin, *Energy Environ. Sci.*, 2014, **7**, 2608–2613.

23 D. Voiry, H. Yamaguchi, J. Li, R. Silva, D. C. B. Alves, T. Fujita, M. Chen, T. Asefa, V. B. Shenoy, G. Eda and M. Chhowalla, *Nat. Mater.*, 2013, **12**, 850–855.

24 A. Ambrosi, Z. Sofer and M. Pumera, *Chem. Commun.*, 2015, **51**, 8450–8453.

25 A. Y. S. Eng, A. Ambrosi, Z. Sofer, P. Šimek and M. Pumera, *ACS Nano*, 2014, **8**, 12185–12198.

26 J. Duan, S. Chen, B. A. Chambers, G. G. Andersson and S. Z. Qiao, *Adv. Mater.*, 2015, **27**, 4234–4241.

27 J. Yang, D. Voiry, S. J. Ahn, D. Kang, A. Y. Kim, M. Chhowalla and H. S. Shin, *Angew. Chemie - Int. Ed.*, 2013, **52**, 13751–13754.

28 T. A. Shifa, F. Wang, Z. Cheng, X. Zhan, Z. Wang, K. Liu, M. Safdar, L. Sun and J. He, *Nanoscale*, 2015, **7**, 14760–14765.

29 T. A. Shifa, F. Wang, K. Liu, Z. Cheng, K. Xu, Z. Wang, X. Zhan, C. Jiang and J. He, *Small*, 2017, **13**, 2–7.

30 J. Lin, Z. Peng, G. Wang, D. Zakhidov, E. Larios, M. J. Yacaman and J. M. Tour, *Adv. Energy Mater.*, 2014, **4**, 1301875.

31 Z. Wu, B. Fang, A. Bonakdarpour, A. Sun, D. P. Wilkinson and D. Wang, *Appl. Catal. B Environ.*, 2012, **125**, 59–66.

32 S. Xu, D. Li and P. Wu, *Adv. Funct. Mater.*, 2015, **25**, 1127–1136.

33 C. Sun, J. Zhang, J. Ma, P. Liu, D. Gao, K. Tao and D. Xue, *J. Mater. Chem. A*, 2016, **4**, 11234–11238.

34 L. Cheng, W. Huang, Q. Gong, C. Liu, Z. Liu, Y. Li and H. Dai, *Angew. Chemie - Int.*

*Ed.*, 2014, **53**, 7860–7863.

35 X. Zhao, X. Ma, J. Sun, D. Li and X. Yang, *ACS Nano*, 2016, **10**, 2159–2166.

36 K. Xu, F. Wang, Z. Wang, X. Zhan, Q. Wang, Z. Cheng, M. Safdar and J. He, *ACS Nano*, 2014, **8**, 8468–8476.

37 F. Wang, J. Li, F. Wang, T. A. Shifa, Z. Cheng, Z. Wang, K. Xu, X. Zhan, Q. Wang, Y. Huang, C. Jiang and J. He, *Adv. Funct. Mater.*, 2015, **25**, 6077–6083.

38 J. Zhang, S. Liu, H. Liang, R. Dong and X. Feng, *Adv. Mater.*, 2015, **27**, 7426–7431.